coatings

MDPI

Article

On the Role of γ-Fe_2O_3 Nanoparticles and Reduced Graphene Oxide Nanosheets in Enhancing Self-Cleaning Properties of Composite TiO_2 for Cultural Heritage Protection

Maryam Mokhtarifar [1], Reyhaneh Kaveh [2], Marco Ormellese [1], Mojtaba Bagherzadeh [2], Maria Vittoria Diamanti [1,*] and MariaPia Pedeferri [1]

1 Department of Chemistry, Materials and Chemical Engineering, Politecnico di Milano, 20124 Milano, Italy; maryam.mokhtarifar@polimi.it (M.M.); marco.ormellese@polimi.it (M.O.); mariapia.pedeferri@polimi.it (M.P.)

2 Department of Chemistry, Sharif University of Technology, Tehran 145888-9694, Iran; reyhanehkaveh@yahoo.com (R.K.); bagherzadeh@sharif.edu (M.B.)

* Correspondence: mariavittoria.diamanti@polimi.it; Tel.: +39-022-399-3137

Received: 7 September 2020; Accepted: 25 September 2020; Published: 29 September 2020

Abstract: The durability of novel metallic artifacts and buildings is an open issue, and the role of smart protecting coatings in extending these artifacts' lifetimes is crucial. In this paper, the role of γ-Fe_2O_3 nanoparticles and reduced graphene oxide (rGO) nanosheets on enhancing the self-cleaning properties of composite TiO_2 films and reducing metal alterations due to contact with acid rain and pollutants is investigated. The photocatalytic assessment of the TiO_2 based films indicates that there are optimum contents for γ-Fe_2O_3 and rGO, which confer the film lower bandgap and tune the TiO_2 anatase/rutile ratio. By adding a proper content of γ-Fe_2O_3, wettability is reduced both in dark and under illumination, which could be related to higher roughness. γ-Fe_2O_3 overloading causes increasing crack density and eventually a fully cracked structure. Adding an appropriate amount of rGO causes a sharp increase in roughness, due to the stacking of rGO nanosheets, while simultaneously avoiding cracking. At higher contents of rGO, wettability further decreases due to higher amounts of hydroxyl groups bound onto rGO; also in this case, overloading causes film cracking. Evaluation of self-cleaning performance and discoloration resistance under soiling and acid rain simulated tests demonstrates that proper loadings of γ-Fe_2O_3 and rGO present higher efficiency thanks to higher superhydrophilic tendency and higher photocatalytic activities, as well as an efficient barrier effect.

Keywords: self-cleaning; discoloration; TiO_2 photocatalyst; γ-Fe_2O_3; reduced graphene oxide; transparent coating

1. Introduction

When it comes to preserving structural integrity and the aesthetic properties of metallic artifacts and cultural heritage, hydrophilic self-cleaning coatings can erect a barrier with significant physicochemical properties to protect them from harsh environments [1]. Indeed, a deep understanding of the structure–function relationship of self-cleaning surfaces is necessary to achieve a suitable wettability and high capability of pollutant photodegradation of the engineered artifacts surfaces. A smart hydrophilic surface could clean a surface by two different approaches: the formation of a sheet of water that washes away dirt (i.e., superhydrophilicity) and the chemical breakdown of adsorbed contaminants on the sunlight irradiated surface (i.e., photocatalysis). The combination of these two

effects is what is generally referred to as self-cleaning. An efficient self-cleaning mechanism can directly lead to prolonged service life as well as to a significant reduction in maintenance costs [2,3]. These considerations apply to all surfaces; the present work focuses specifically on metallic ones, where not only soiling can impair surface aesthetic properties, but also corrosion can damage, irreversibly, the metallic artifact exposed to the atmosphere, especially in polluted environments where acid rains are present.

The role of these protecting coatings becomes more notable when it comes to the protection of valuable metallic based artifacts made by novel metals such as aluminum, stainless steel, and titanium exposed to environmental pollution with a heavy impact on their surface conditions, including discoloration. Although discoloration does not necessarily affect the metal mechanical stability, it impairs the aesthetic appearance of metallic buildings and artifacts, hence posing a limit to their functionality, which is strongly related to their appearance [4]. In the case of titanium sheets exposed to the outdoor environment, atmospheric discoloration mainly occurs because of the reaction of acid rain with impurities introduced in the titanium surface during the manufacturing process, resulting in the oxidation of titanium and consequent thickening of the natural oxide layer, responsible for the appearance of various surface colors [5–7]. Figure 1 shows different parts of a gray color titanium sheet exposed to exterior cladding; a building located in Taiwan. As it is clear, the sheet lost its color originality through oxidizing in the harsh environment resulting in a variety of colors and thicknesses on the surface.

Some general features desired in the design of smart hydrophilic coatings to preserve artifacts are the following: low number of additives, wettability, durability, proper adhesion, chemical stability, as well as transparency to maintain the original surface aesthetic characteristics [1,8].

In the case of metal oxide coatings, an effective protection to the metal substrate can be provided upon the implementation of SiO_2, ZrO_2, Al_2O_3, CeO_2, and TiO_2 due to their high chemical stability. Among them, the optically transparent, superhydrophilic, and photocatalytic TiO_2-based coatings are widely used in buildings and artifacts preservation as TiO_2 exhibits significantly high physical and chemical stability, low cost, easy availability, low toxicity, and excellent photoactivity [8–10]. Moreover, the photoactivity of TiO_2 could be improved by shifting the light absorption spectra from UV to the longer wavelengths of visible light range, which is achieved by doping with metals [11–14], or by forming heterojunctions between TiO_2 and a lower bandgap semiconductor [15–17]. Moreover, high surface area materials, such as carbon-based materials, can be used to boost photoactivity performance through increasing available surface sites [18,19].

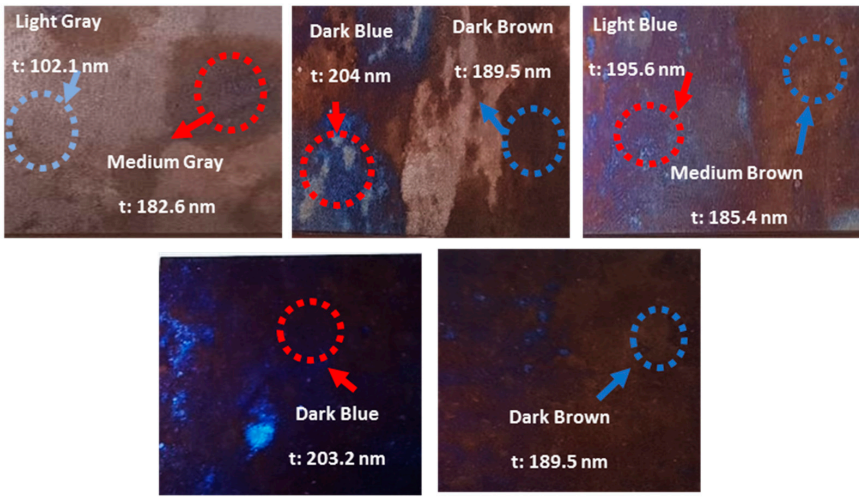

Figure 1. Color changing due to the formation of oxide films with a variety of thicknesses (*t*) in different parts of a titanium sheet used as exterior cladding of a building located in Taiwan.

In our previous work, the synthesis and characterization of a novel composite containing (optimized) $TiO_2/SiO_2/\gamma$-Fe_2O_3/rGO was reported, and its efficiency in discoloration resistance of metallic artifacts was discussed [20]. Since it is critical to understand the role and appropriate content of γ-Fe_2O_3 nanoparticles and rGO nanosheets, in this work, we analyzed the optimal content of both additions, discussing mechanisms activated by insufficient loading or overloading in the enhancement of self-cleaning properties, morphology, and protection of metallic cultural heritage.

2. Materials and Methods

2.1. Materials

All chemicals—iron chloride tetrahydrate ($FeCl_2$, $4H_2O$), propylene oxide, tetraethyl orthosilicate (TEOS), tetrabutyl titanate (TBT), sulfuric acid (H_2SO_4), ethanol (C_2H_5OH), and methylene blue (MB)—were purchased from Sigma–Aldrich and used as received. Gamma Fe_2O_3 (γ-Fe_2O_3) nanoparticles were prepared by dissolving $FeCl_2{\cdot}4H_2O$ (5 mmol) in ethanol (0.3 M) and then adding propylene oxide (50 mmol), sonicating for 15 min and stirring for 6 h. The resulting solution was heated at around 100 °C to evaporate the solvents, leaving a brown powder.

Silica (SiO_2) was prepared by adding TEOS (40 mmol) to 65% HNO_3 and stirring the solution for 1 h (molar ratio of TEOS and H^+ was kept 2.4) followed by centrifugation and drying at room temperature for 10 h. The obtained powder was dissolved in 10 mL of ethanol under sonification for 1 h, and then propylene oxide (400 mmol) and TBT (40 mmol) were added to the solution to form Solution A, that was then aged for 72 h. Finally, the solution was mixed with different contents of as prepared γ-Fe_2O_3 nanoparticles (0.016, 0.032, and 0.063 g), and the mixtures were sonicated for 1 h. To prepare rGO sol-gels, different loadings (0.01, 0.02, and 0.03 g) of rGO were added to the $TiO_2/SiO_2/Fe_2O_3$ with 0.032 g γ-Fe_2O_3, followed by stirring for 2 h. For the sake of comparison, two separate solutions, including only TiO_2 and TiO_2/SiO_2, were prepared as well.

To evaluate the coating characteristics, metallic titanium specimens, grade 2 following ASTM classification, were coated with the TiO_2, TiO_2/SiO_2, $TiO_2/SiO_2/\gamma$-Fe_2O_3, $TiO_2/SiO_2/\gamma$-Fe_2O_3 (0.032 g)/rGO sols (with abbreviation names TS, TSF, and $TSF_{32}G$ for three last sols, respectively) by dip-coating. The number of dips was always set to be two, and the immersion rate was kept at 200 mm/min while the withdrawal rate was modulated at 100 mm/min with dipping angles of 90 degrees. To have coated substrates with the same geometric area, a selected area of 1.7×1.9 cm^2 was exposed by covering the rest of the sample with Kapton tape. Drying was done in ambient conditions for 24 h between the two dipping steps, followed by calcination at 600 °C for 2 h (Figure 2a). FESEM morphology images of a $TSF_{32}G$ thin film (as an example) are presented in Figure 2b. The $TSF_{32}G$ thin film shows a clearly uniform structure with average thickness 340 nm.

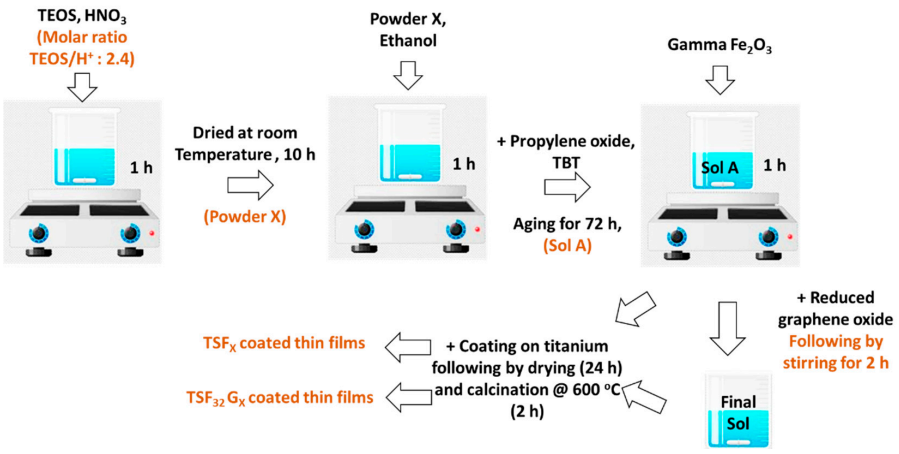

(**a**)

Figure 2. *Cont.*

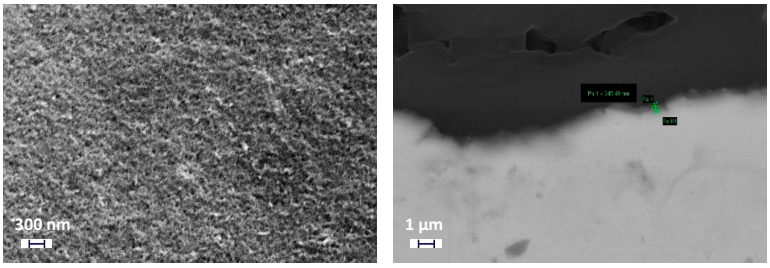

(**b**)

Figure 2. (**a**) Schematic illustration of the synthesis of the sol gels and preparation of the coated films, (**b**) SEM images of structure and thickness of the $TSF_{32}G$ thin film.

2.2. Characterization Techniques

The sol-gel coated samples were characterized using X-ray diffraction analyses (XRD), Fourier transform infrared (FTIR) spectra, atomic force microscopy (AFM), and UV-Vis-NIR diffuse reflectance spectra to understand their structures and optical properties, which influence photocatalytic performances.

Specifically, XRD was used to investigate the coating crystallinity; diffraction patterns were recorded on a Philips PW1830 powder diffractometer (Amsterdam, The Netherlands) operating at 40 kV voltage and 40 mA filament current. Spectra were acquired at the scanning rate of 2.5° per minute with Cu Kα1 radiation in the 2θ range 20°–60°. Optical properties were investigated by UV–Vis-NIR diffuse reflectance. Spectra were recorded in the 220–2600 nm range with a Shimadzu UV 3600 Plus spectrophotometer (Shimadzu, Kyoto, Japan) equipped with an ISR-603 integrating sphere, and $BaSO_4$ was used as reference material. The bandgap was calculated after Kubelka–Munk conversion using the Tauc plot method [21,22]. FTIR spectra of the prepared samples were recorded on a Bruker Tensor 27 spectrometer (Billerica, MA, USA) using a KBr pellet for sample preparation at room temperature. Surface roughness of the coated samples was studied by atomic force microscopy (AFM) using an NT-MDT AFM (Zelenograd, Moscow, Russia) Solver Pro apparatus operating in contact scanning mode by means of 60×60 mm^2 AFM images. Photocatalytic activity was evaluated in the degradation of Methylene Blue (MB), observed as the variation of its absorbance upon exposure to UV light in presence of the photoactive coating. MB absorbance was measured at given time intervals of irradiation by spectrophotometry (UV–vis spectrophotometer, Thermo scientific Spectronic 200E) at l = 668 nm, where MB has its maximum absorbance. Before photodegradation, the specimens were kept in the dark for 50 min to reach adsorption–desorption equilibrium. The samples were then illuminated for 330 min in an aqueous MB solution (10^{-5} M, 40 mL) under UV LED (450 mW, 500 mA, 3.8 V, 300–400 nm) and visible LED (4.62 W, 700 mA, 3 V, 400–800 nm) at a 3 cm distance with the light sources.

The onset of superhydrophilic behavior was evaluated by measuring surface contact angle; this was performed by placing a droplet of distilled water on the surface on five predefined positions on the coating substrates and recording the resulting image by a CCD camera connected to the computer via a PCI card. Before measurements, the plates were kept in the dark for 24 h to ensure that contact angles in dark were not affected by ambient light. Then, the specimens were put under irradiation with a simulated solar light (intensity ~4500 µW/cm^2) for 30 min, and their contact angles were measure immediately. Contact angles were measured both before and after simulated solar light exposure.

Four soiling agents, presented on urban surfaces, were selected to mimic natural soiling, including black carbon, mineral dust, humic acids (organics), and inorganic salts. These soiling agents were mixed in different ratios in an aqueous mixture and applied on the bare and coated surfaces by dip deposition with a 45° dipping angle. These individual components were optimized to reproduce roofing products exposed in marine and urban polluted environments [22,23] (Figure 3).

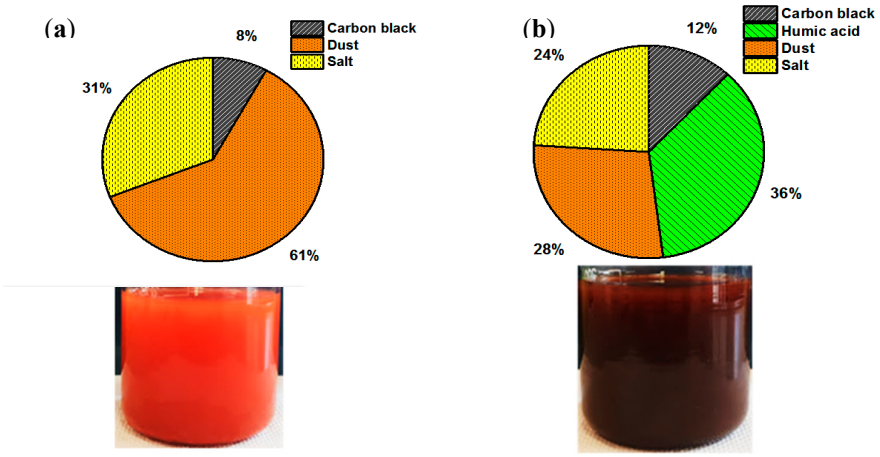

Figure 3. Volume fractions and their color of artificial soiling mixtures including carbon black, humic acid, dusts, and salts used to mimic the soiling of roofing materials, (**a**) marine, and (**b**) urban polluted environments.

Before starting the process, specimens were put under simulated solar light for 1 h to induce photoactivation and then dipped in the soiling components immediately. Then, the soiled plates were left to be entirely dried, and their color changes due to soiling were measured by spectrophotometry (Konica Minolta spectrophotometer CM-2500d, Tokyo, Japan) to evaluate their self-cleaning ability. Colorimetric measurements were analyzed in terms of color difference ($\Delta E = \sqrt{((\Delta L^*)^2 + (\Delta a^*)^2 + (\Delta b^*)^2)}$) to study the coated films color variation, according to the CIEL*a^*b^* color system.

To estimate the discoloration resistance of the coated titanium pieces, the samples were immersed and kept in solution with pH 4—adjusted with certain amounts of sulfuric acid and sodium hydroxide—(at 65 °C temperature for 7 days) as an accelerated acid rain simulation.

3. Results

3.1. Structural Study of the Coated Films

As presented in our previous work, the starting morphology of the sol before the addition of iron and graphene oxides is represented by the TS samples, where TiO_2 nanoparticles with mixed anatase–rutile phases distribute over the larger amorphous SiO_2 particles. XRD patterns of the TSF and $TSF_{32}G$ coated samples calcined at 600 °C are presented in Figure 4. With increasing γ-Fe_2O_3 content, anatase TiO_2 peaks decrease while peaks for the rutile phase are clearer. This observation indicates that at certain threshold Fe(III) ions have a substantial influence on the anatase TiO_2 phase at the interface of (TiO_2/SiO_2) and γ-Fe_2O_3 compounds, facilitating the anatase–rutile phase transformation [24–26]. Indeed, since the ionic radius of Fe^{3+} (0.64 Å) is similar to the ionic radius of Ti^{4+} (0.68 Å), the incorporation of Fe in the matrix of TiO_2 is possible, and the presence of such defects in TiO_2 crystals might have facilitated the anatase–rutile transition (Table 1) [27,28].

Table 1. Anatase/rutile percentage and particle size (nm) in the TSF and $TSF_{32}G$ coated films.

Sample	Anatase/Rutile (%)	Particle Size (nm)
TSF_{16}	80/20	22.8
TSF_{32}	60/40	24.1
TSF_{63}	53/47	25.5
$TSF_{32}G_1$	67/33	23.9
$TSF_{32}G_2$	70/30	23.3
$TSF_{32}G_3$	75/25	24.5

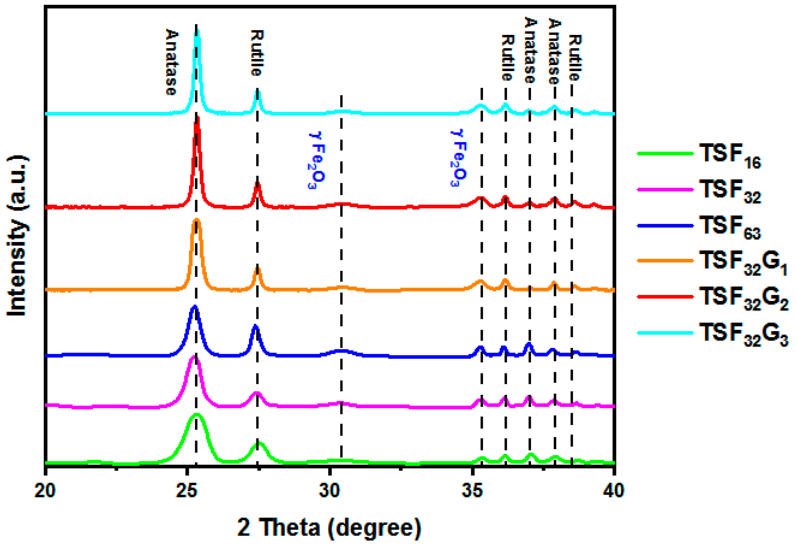

Figure 4. XRD pattern of the TSF and TSF32G coated films after heat treatment at 600 °C.

On the other hand, an opposite effect was found in $TSF_{32}G$ films, as the anatase/rutile ratio increased by adding rGO in the sol; hence the presence of carbon retarded the anatase–rutile transformation (Table 1). This may be attributed to the high surface area of rGO, as well as to a reduction in acidity and promotion of the dehydration of Ti^{4+} complex by forming edge shared bonds [29–31]. Indeed, a variation in the number of OH ligands in the Ti complex produced from Ti^{4+} hydrolysis was observed to change acidity [32–34].

Figure 5 shows the FT-IR spectra of the TSF, and $TSF_{32}G$ coated films in the wavenumber range from 300 to 4000 cm^{-1}. As observed in our previous work, the TiO_2 sample shows three bands: the first broad absorption band at around 3500 cm^{-1} corresponding to the stretching vibration of the hydroxyl group O–H of TiO_2. The second absorption band at 1627 cm^{-1}, related to bending modes of Ti–OH, indicates surface hydroxylation of nanoparticles, and another band at 1381 cm^{-1} is attributed to Ti–O modes. The interaction between TiO_2 and SiO_2 in the TS was exhibited in the Ti–O–Si bond (~970 cm^{-1}) [35–37]. The absorption band at 1104 cm^{-1} correlated to Si–O–Si, corresponding to its asymmetric stretching vibration. Furthermore, two peaks at around 453 and 544 cm^{-1} can be observed for the γ-Fe_2O_3 sample, corresponding to Fe–O groups, which exhibited a slight blue shift in the case of the TSF and $TSF_{32}G$ films, possibly due to surface augmentation by γ-$Fe_2O_3$and rGO [25,36]. Eventually, in the $TSF_{32}G$ films, the absorption peak at 1542 cm^{-1} could be assigned to the skeletal vibration of unoxidized graphitic domains or bending vibration of the H_2O molecule present in GO [35,36]. Furthermore, with increasing the loading of rGO from 0.01 to 0.03 g, relative intensities of these peaks also increased.

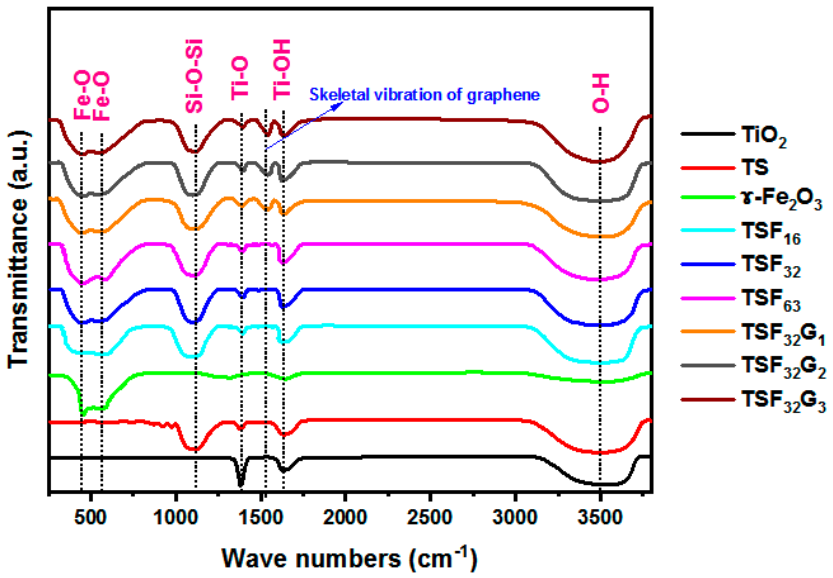

Figure 5. FT-IR spectra of the TiO_2, TS, γ-Fe_2O_3, TSF, and $TSF_{32}G$ coated films in the wavenumber range from 300 to 4000 cm^{-1}.

3.2. Monitoring Self–Cleaning Properties through Photoactivity Variations under UV and Visible Lights

A plot of the transformed Kubelka–Munk function as a function of energy of light is shown in Figure 6, by which the roughly estimated band gaps were 2.91, 2.87, 2.88, and 2.81 eV corresponding to TSF_{16}, TSF_{32}, and TSF_{63}, respectively. The bandgap values are decreased to 2.71, 2.26, and 2.67 eV by adding rGO with 0.01, 0.02, and 0.03 g. It means that the addition of rGO (especially up to 0.02 g) induced a redshift to higher wavelengths in the absorption edge in the UV and visible light regions. This result indicated that a narrowing of the bandgap in the $TSF_{32}G_2$ sample than TiO_2. The narrowing should be attributed to the chemical bonding, including the formation of the Ti–O–C bond between TiO_2 and rGO [37,38].

To explore the influence of Fe_2O_3 and rGO on TiO_2 composite films, the photocatalytic activity of TSF and TSFG-coated films for UV and visible-light-driven degradation of MB was performed at room temperature and under ambient pressure (Figure 7a,b). For comparison, the direct photolysis of MB and photocatalysis with pure TiO_2 and TS coated films were also performed. The equilibrium adsorption state in dark confirmed that MB adsorption on all the samples was negligible. A control experiment in the absence of any photocatalyst under otherwise identical conditions shows that negligible activity was observed under light irradiation. The results demonstrated good linearity of ln C/C_0 vs. time, with R-squared values (R^2) higher than 0.9, confirming the correct choice of pseudo-first-order kinetics model for the photocatalytic reactions [38,39]. The kinetic constants (k) and degradation extents of the TiO_2, TS, TSF, and $TSF_{32}G$ films deposited on titanium substrate are reported in Table 2. As depicted in Figure 7a, pure TiO_2 degraded only 32% of MB after 6 h under UV irradiation, while TiO_2–Si degraded about 53% of MB in the same condition. The addition of γ-Fe_2O_3 led to a significant improvement, increasing the final degradation extent to 66% at the minimum iron oxide content and 76% at the optimal content of 0.032 g. The further addition of an optimal content of rGO—i.e., 0.02 g—also improved the photocatalytic behavior, reaching a photocatalytic degradation of 83%. Under visible light, excellent improvements were obtained compared to pure TiO_2 (5%), reaching 53% and 70% in the same optimized compositions (Figure 7b). Indeed, among TSF coated films, TSF_{32} demonstrates a higher photoactivity, in spite of no significant differences between the bandgaps in 0.032 and 0.063 g γ-Fe_2O_3 contents. Hence, the better performance should be related not only to proper bandgap, but also to optimal anatase/rutile ratio (60:40) [39–42]. Moreover, in comparison with the pure TiO_2 and TS films, adding a proper amount of γ-Fe_2O_3 could improve charge separation and reduce recombination, since the conduction band (CB) potential of γ-Fe_2O_3 is

more negative than that of TiO_2, hence photo-generated electrons in TiO_2 could transfer to the surface of γ-Fe_2O_3 and photo-generated holes in the valence band (VB) of γ-Fe_2O_3 could migrate to TiO_2, simultaneously [42–45].

The presence of rGO further improved photocatalytic performances compared to the TSF films. The formation of the Ti–O–C bond resulted in a redshift in the absorbance edge of TiO_2, causing an increase in bandgap (Figure 6). Moreover, the two-dimensional structure of the rGO nanosheet and its electrical transport property could boost light absorption and electron transfer in the $TSF_{32}G$ films, improving the separation of the electron-hole pairs. More specifically, the photocatalytic degradation ratio of MB under both UV and visible lights followed the order $TSF_{32}G_2$ > $TSF_{32}G_3$ > $TSF_{32}G_1$. Indeed, at higher rGO loading (0.03 g), the black rGO sheets would increase photo absorption and scattering and, at the same time, reduce the contact surface of TiO_2 with light irradiation, leading to a decrease in photodegradation [39,40]. For comparison, recent reports on the self-cleaning properties of different coated films are listed in Table 3.

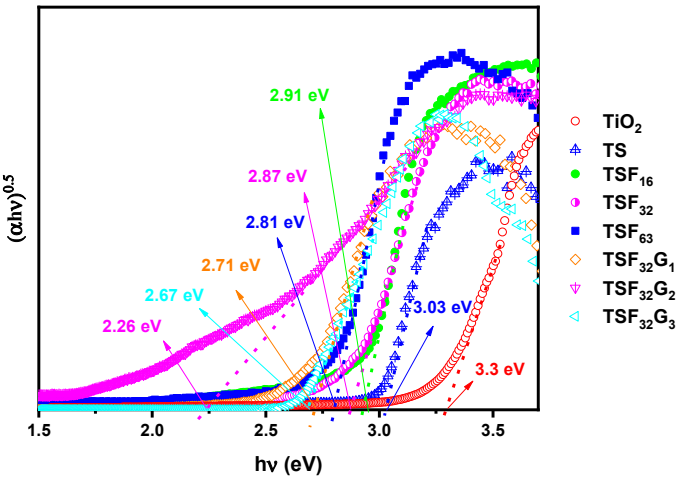

Figure 6. Tauc plots of $(\alpha h\nu)^{0.5}$ versus hν were employed to estimate the band gaps of the TiO_2, TS, TSF, and $TSF_{32}G$ coated films with different loadings.

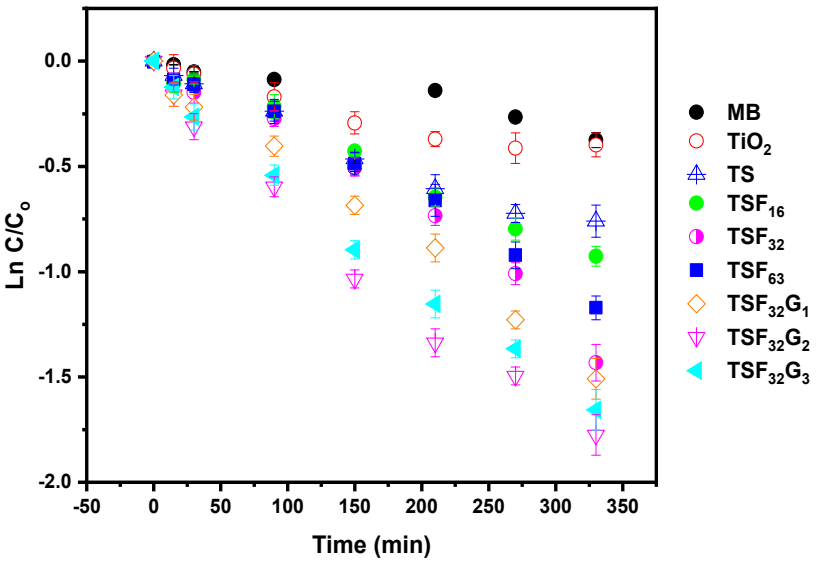

(**a**)

Figure 7. *Cont.*

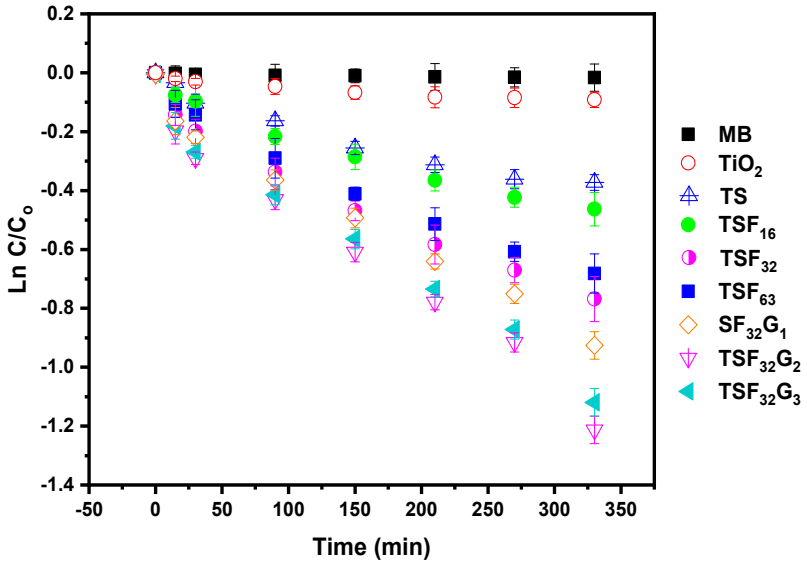

(**b**)

Figure 7. The photocatalytic activity for degradation of MB under (**a**) UV and (**b**) UV-Vis lights for TiO_2, TS, TSF, and $TSF_{32}G$ coated films.

Table 2. Kinetic constants of photocatalytic MB degradation under UV and vis lights for TiO_2, TS, TSF, and $TSF_{32}G$ coated films, plus degradation extent after 330 min test.

Sample	UV			UV-Vis		
	K (min^{-1})	R^2	Degradation (%)	K (min^{-1})	R^2	Degradation (%)
MB	n/a	0.95	1.7	n/a	0.93	1.6
TiO_2	−0.0013	0.93	32.0	n/a	0.91	5.2
TS	−0.0024	0.98	53.2	−0.0012	0.94	31.1
TSF_{16}	−0.0028	0.99	66.4	−0.0013	0.96	37.1
TSF_{32}	−0.0038	0.95	76.1	−0.0021	0.96	53.6
TSF_{63}	−0.0034	0.99	69.0	−0.0019	0.97	49.4
$TSF_{32}G_1$	−0.0042	0.99	77.9	−0.0023	0.99	60.4
$TSF_{32}G_2$	−0.0053	0.98	83.0	−0.0032	0.98	70.3
$TSF_{32}G_3$	−0.0047	0.99	80.9	−0.0026	0.99	67.3

Table 3. Self-cleaning performance of different coated films.

Composite	Light Source	Soiling Method	Degradation Extent and Time Required	Concentration
Graphene-loaded TiO_2 [41]	UV light	MB	85%-20 h	0.01 mM
$VO_2/SiO_2/TiO_2$ [42]	UV light	Stearic acid	40%-50 h	Dip-coated of a layer of stearic acid onto the films from a chloroform solution (0.05 M)
Au/TiO_2-covered cellulose fiber [43]	Solar light	MB	95%-10 h	4.0 mg/g of cotton fiber
SiO_2–TiO_2 [44]	UV light	RhB	80%-35 h	15 mL, 1 ppm
TiO_2 [45]	UV light	RhB	80%-24 h	0.1 mmol/L
TiO_2 [46]	UV light	RhB	100%-9 h	2.6×10^{-3} M
TiO_2 [47]	UV light	MB	40%-24 h	0.5 mL, 100 µmol/L
TiO_2 [48]	Sunlight	RhB	90%-7$\frac{1}{2}$ h	0.05 g/L
TiO_2 [49]	Xenon lamp	RhB	85%-7$\frac{1}{2}$ h	0.05 g/L
TiO_2 [50]	UV light	Organic dye	100%-25 h	1 mg/mL

3.3. Self-Cleaning and Discoloration Resistance Evaluations

3.3.1. Roughness, Transparency, Color Changing, and Coated Film Integrity

The average roughness (R_a) of the substrates coated with TiO_2, TS, TSF, and $TSF_{32}G$ films are presented in Table 3. It is confirmed that R_a has an intense enhancement in the case of TS and TSF with respect to pure TiO_2 films, especially with the addition of the optimal amount of γ-Fe_2O_3, where R_a has a peak value of about 69 nm, while this parameter is about 51 and 57 nm for TSF_{16} and TSF_{63}, respectively. Adding 0.02 g rGO causes a sharp increase in roughness due to the sloppy stacking of rGO sheets, which creates some large channels around the rGO stacks, while a lower amount of rGO does not have significant impact. The presence of stacks may be correlated to the fact that rGO sheets assemble in random order, inconsistent with the change in surface roughness [51–54]. However, overloading rGO in the $TSF_{32}G_3$ coated film resulted in a decrease in roughness probably due to channels covering around the rGO stacks (Figure 8).

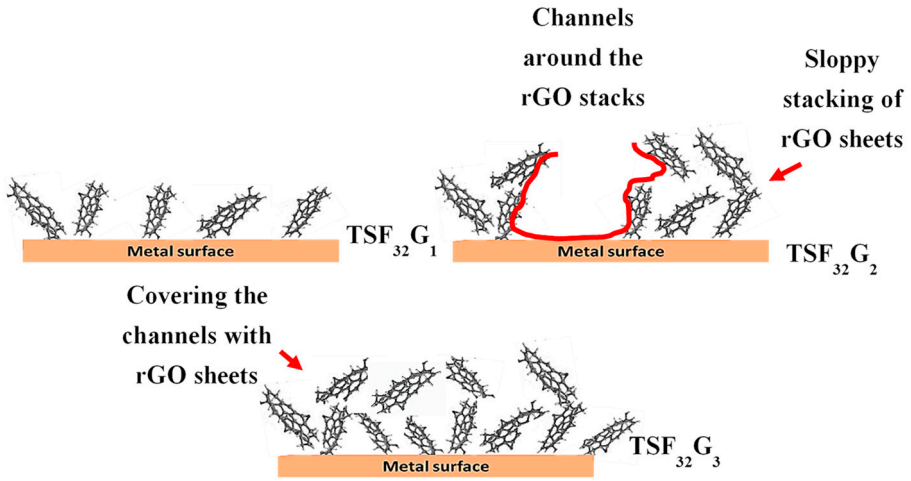

Figure 8. A schematic of the effect of rGO loading on the roughness of the $TSF_{32}G$ coated films.

Transmittance in the range 300 to 800 nm was measured on coated glass slides, as presented in Table 2. Except for TSF_{63} and $TSF_{32}G_3$ coated films, all other specimens show a high transparency of up to 80%. Although transmittance slightly decreased, with the addition of γ-Fe_2O_3 and rGO, samples are still satisfactory from an aesthetic viewpoint. Generally, the increased surface roughness in TSF_{32} and $TSF_{32}G_2$ coated films could be responsible for the slight loss in optical transmission compared with TiO_2 and TS coatings, together with the possible absorption in visible light for both γ-Fe_2O_3 and rGO, which both present dark colors when considered in bulk.

To further analyze this aspect, colorimetric measurements were carried out on the uncoated and coated glasses with TiO_2, TS, TSF, and $TSF_{32}G$ coated films (Table 4). The pure TiO_2 coating did not alter the aesthetic appearance of the specimen, with $\Delta E < 1$, meaning it is not perceivable by human eyes. By adding other compounds, SiO_2 and particularly γ-Fe_2O_3 up to 0.032 g, ΔE values increased to about 2 ($\Delta E \leq 2$), still indicating differences negligible to human eyes. However, adding the highest amount of γ-Fe_2O_3 caused a significant increase in ΔE to 4.6, which is perceivable through close observation. On the other hand, also rGO up to 0.02 g does not have significant effects on color, while at its highest amount ΔE exceeded 3, meaning that differences could actually be observed.

Table 4. Average surface roughness R_a, transmittance in the region 380–740 nm, and ΔE caused by TiO_2, TS, TSF, and $TSF_{32}G$ coated films with different loadings.

Parameter	Glass	TiO_2	TS	TSF_{16}	TSF_{32}	TSF_{63}	$TSF_{32}G_1$	$TSF_{32}G_2$	$TSF_{32}G_3$
Average Roughness (R_a) (nm)	-	40	47	51	69	57	67	200	177
Transmittance (%)	98	95	93	89	87	71	84	81	41
Color difference (ΔE)	0	0.5	1.28	1.56	2.16	4.69	2.39	2.65	3.2

3.3.2. Monitoring of Self-Cleaning Property through Contact Angle Changing

As a key parameter in self-cleaning, wettability was analyzed by measuring water contact angle (CA) on the coated surfaces. Wettability is highly dependent on chemical composition and structure of the coated surfaces [55–57]. Water CAs of TiO_2, TS, TSF, and $TSF_{32}G$ coated surfaces were measured in the dark and after 30 min light irradiation. CA values are given in Figure 9. In particular, the TiO_2 film shows a CA above 90°, which is kept almost constant even after illumination, confirming a poor wetting due to a slightly hydrophobic surface. However, by adding SiO_2 both in the dark and after exposure to light hydrophilicity increased, due to the Si–O–Ti bonds (present in the FTIR spectrum (Figure 5)) at the interfaces, whose acid character may induce a higher amount of hydroxyl groups at the film surface [58–61]. In addition, the hydrophilic tendency in the TS thin film could be due to a retarding effect on anatase-to-rutile phase transformation and the crystal growth of anatase by adding SiO_2, as discussed above (Figure 4), as it is known that anatase can accommodate more OH groups compared with rutile [62].

By adding γ-Fe_2O_3 up to 0.032 g, wettability was improved both in the dark and under illumination (CA_{light}: CA_{Dark} 50°: 68° and 35°: 55° for 0.016 and 0.032 g, respectively). However, these values both increased again by adding γ-Fe_2O_3 up to 0.063 g. Indeed, Fe^{3+} ions act as both photo-generated holes and electron traps and to impede the hole–electron recombination (see Figure 10; Equations (1) and (2)) [63]. The products of these two reactions (Fe^{4+} and Fe^{2+} ions) are relatively unstable oxide forms of Fe than Fe^{3+} ions, so that trapped charges can transfer from Fe^{4+} and Fe^{2+} to the interface to participate in redox reactions [64,65] (Equations (3) and (4)), resulting in the oxidation of lattice O_2^- anions by more photo-generated holes, following more oxygen vacancies. Consequently, these oxygen vacancy sites may be coordinated by water molecules and lead to their adsorption on the TSF thin film surfaces [66]. By adding different contents of rGO to the TSF_{32} sol, CAs decrease even more, both in the dark and under light, changing from hydrophilic to superhydrophilic. The enhancement of the hydrophilic conversion rate is ascribable to hydrophilic functional groups bound onto rGO [67], to the improvement in charge separation efficiency as the rGO layer may work as an electron acceptor, and to the increased roughness, typical of a Wenzel state, which leads to higher –OH adsorption sites from water molecules [68–72]. The rGO nanosheets could turn wettability to superhydrophilicity, as oxygen on graphene have a higher energy state [73,74], resulting in a depletion of a large number of oxygen atoms, which in turn results in a continuous diffusion of oxygen vacancies on the rGO surface. Consequently, water molecules in air capture the oxygen vacancies and generate OH radicals binding to the graphene carbon atom in a supramolecular form [74,75] (Figure 10, Equations (5)–(8)).

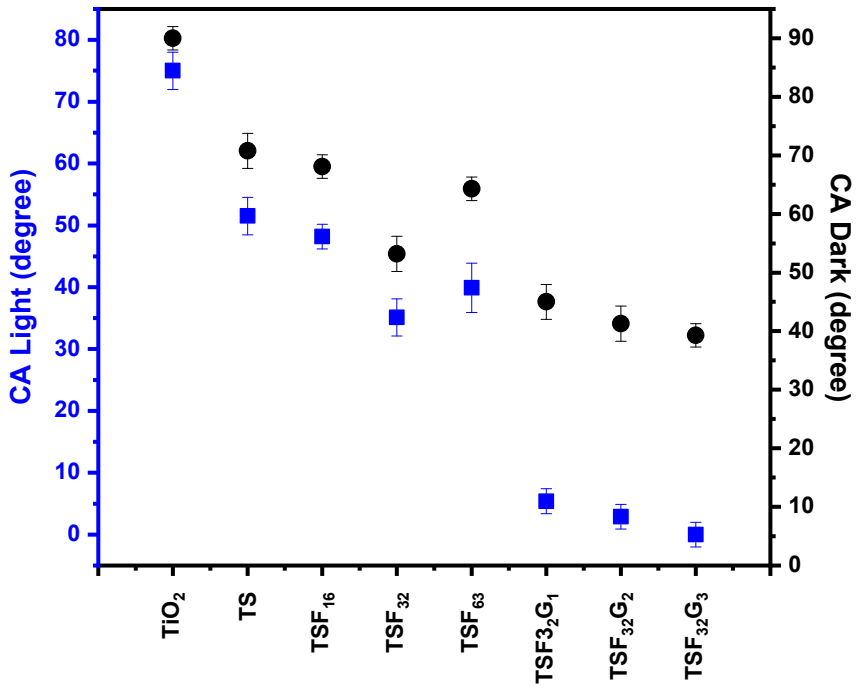

Figure 9. Water contact angle (CA) images of the coated films on the titanium substrate in the dark and under illumination.

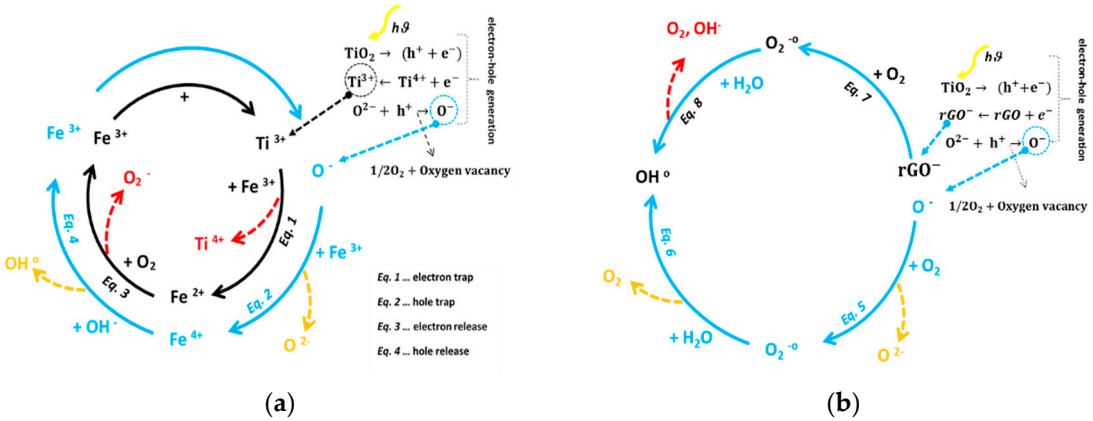

Figure 10. The proposed mechanisms for turning to hydrophilicity in TiO_2 affected by (**a**) γ-Fe_2O_3, (**b**) rGO.

The morphological changes observed during dip coating and then drying of a film are due to the combined effects of the capillary stress and the presence of the lowermost layer of the particles near the substrate that oppose to the relaxation of the generated stress. This leads to the dissipation of the stress through the creation of cracks. Generally, the improvement in interfacial adhesion stability of a film could be related to better interactions between coated layers and substrate. It is confirmed that adding SiO_2, Fe_2O_3, and GO to TiO_2 thin films could improve adhesion [76–83]. Moreover, it is widely accepted that the presence of the cracks can have a negative impact on photoactivity and wettability properties, and so crack-free coated films are highly appreciated. However, it is very important to consider the effect of different crack characteristics, such as density, number, homogeneity, orientation, and connection between cracks in thin films [84]. Consequently, the connection of nanoparticles in the coated films is affected by the cracks' characteristics in terms of width, density, and morphology through the reduction in the path lengths of electron transport within the nanoparticle networks. Generally, thin films with several cracking directions and connections show an electron disconnection

in a relevant part of the film, which drastically reduce the photocatalyst efficiency. Conversely, cracks that do not electronically separate film parts have a minor effect on the efficiency [85,86].

In Figure 11, it can be seen clearly that loading more γ-Fe_2O_3 in the TSF films showed increasing crack density in a way that crack growth in the TSF_{63} cause a fully cracked structure. Conversely, adding rGO upon 0.02 g resulted in crack free coatings, improving the stability of the thin film through making a dense structure. However, increasing rGO content to 0.03 g adversely affects the stability of the $TSF_{32}G_3$ film, leading to crack propagation in the structure. On the other hand, if the structure of the coated films is considered, crack characteristics are completely different for the prepared films (see schematic Figure 12). It could be useful and interesting to understand how different loadings of γ-Fe_2O_3 and rGO consequently affect propagation and type/shape of cracks and self-cleaning properties. In the TSF_{32} film (also in the TSF_{16}), cracks' characteristics are different in terms of small width and both are interconnected and isolated cracks. In this case, cracks' characteristics do not promote electron disconnection in the photoactive TSF_{32} film. For the TSF_{63} coated film, the cracks' widths are very polydisperse, and their density is high with intersections leading to interconnected cracks. Additionally, the large crack widths reduce the probability of the pollutants to come into contact with the coated substrate, reducing efficiency as well [87]. Crack connections may also promote the formation of large dense domains, helping light scattering and reducing light harvesting. Conversely, a dense structure limits the electron path transport toward the substrate, which reduces the probability of the recombination process to occur [83,88]. The balance between all abovementioned phenomena contribute to obtain lower efficiency in the TSF_{63} film, and better efficiency in the dense, crack-free $TSF_{32}G_1$ and $TSF_{32}G_2$ coated films.

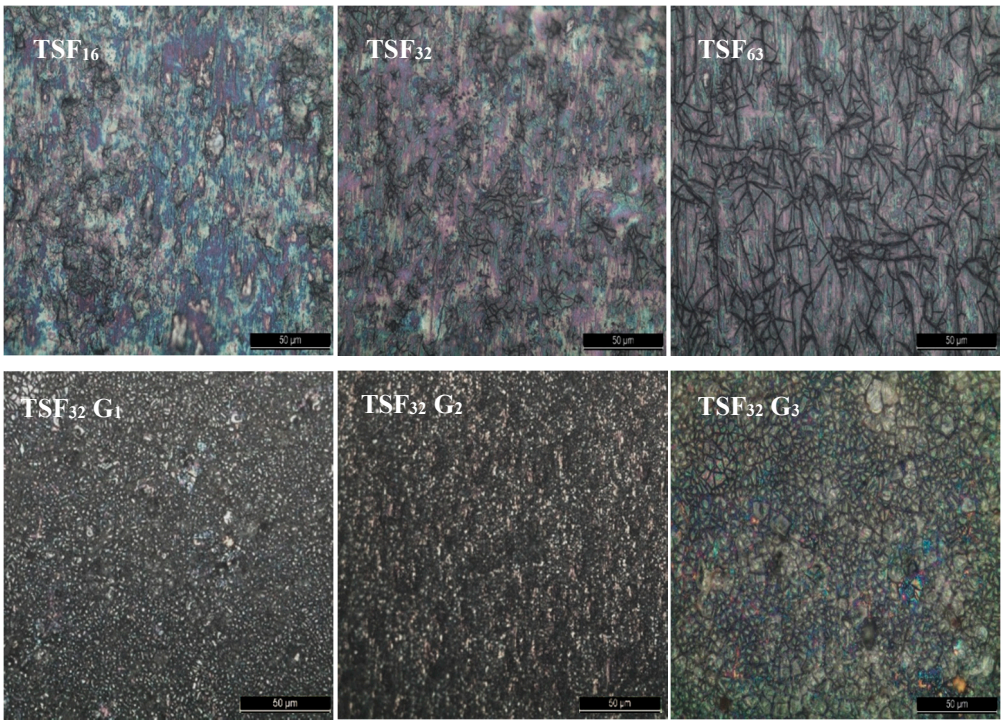

Figure 11. The optical microscopy images of the structure of the TSF and $TSF_{32}G$ coated films.

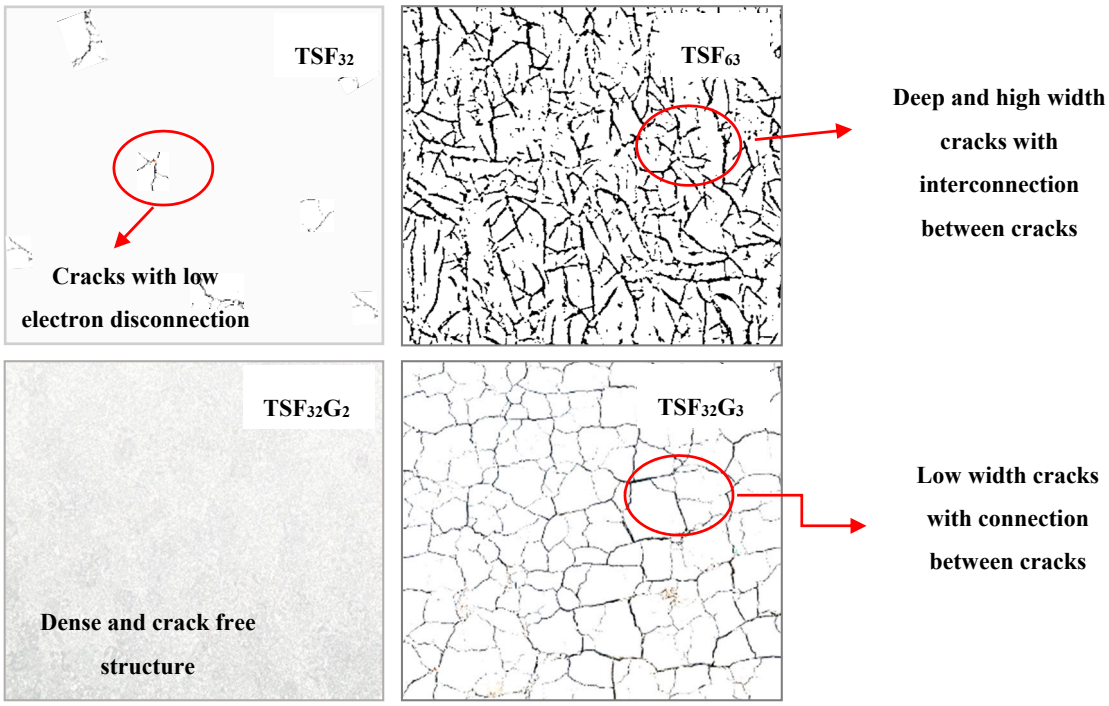

Figure 12. Schematic presentation of type and density of cracks in the TSF_{32}: island structure, TSF_{63}: branch structure, $TSF_{32}G_2$: dense structure, and $TSF_{32}G_3$: honeycomb structure coated films.

3.3.3. Effect of γ-Fe_2O_3 and rGO in Maintaining the Original Color of the Coated Films in Harsh Environments

As previously mentioned, the original color of a metallic substrate could easily be changed through exposure to aggressive environments, such as acidic media or due to deposition of dust, fly ash, soot, or other particulate matter suspended in air. Here, we examine how γ-Fe_2O_3 and rGO loading could preserve the surface by using both simulated acid rain and soiling tests.

Figure 13 shows the effect of the artificial acid rain solution with pH 4 on titanium specimens discoloration after 7 days immersion. The original color of bare Ti was strongly affected, with a ΔE value of 11, meaning severe discoloration after one week and then a stabilization, which might be attributed to a slower dissolution of TiC as the main contribution to discoloration in acid environments [7]. On the other hand, coated specimens showed a lower Δ*E*. Only in TSF16 and TSF63 coated specimens, the color differences were close to 5 and 4, respectively, meaning that their color changes due to discoloration could be seen by the naked eye. The optimized content of γ-Fe_2O_3 (0.032 g) showed a Δ*E* below 3. Moreover, rGO could protect the metal surface from discoloration significantly, even at low amounts. Only in case of a too high amount of rGO some discoloration could take place, as the coating is likely damaged by rGO overloading.

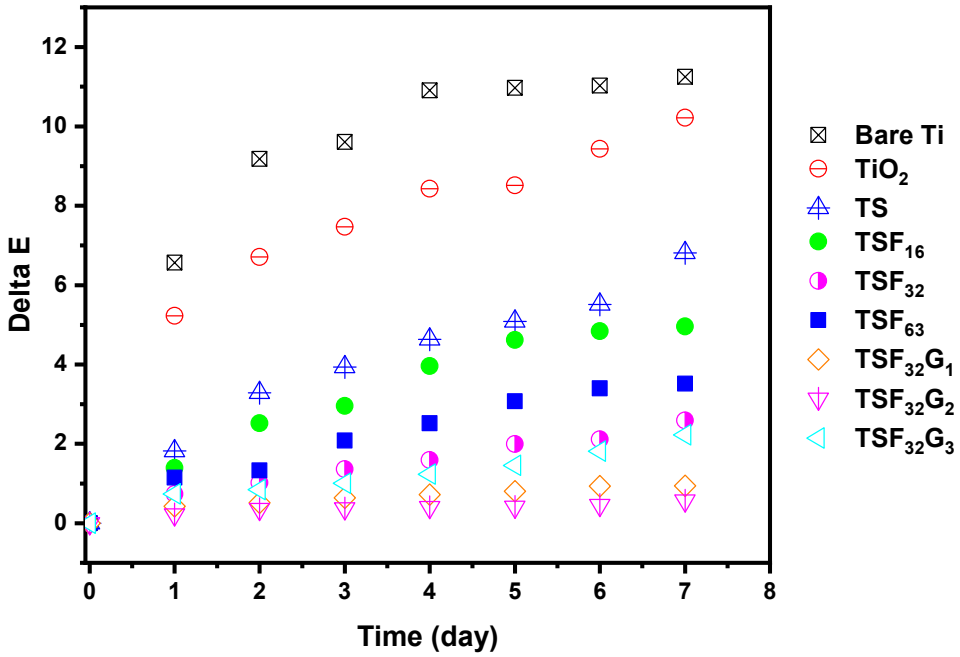

Figure 13. The discoloration test results of the bare and coated titanium specimens with the TiO_2, TS, TSF, and $TSF_{32}G$ samples in an acid solution of pH 4 at 65 °C.

The color difference caused by applying the simulated soiling test is presented in Figure 14. As expected, all the coated specimens showed lower ΔE than the bare one; specifically, the TSF_{32} coated film better preserved the surface conditions compared to other TSF thin films, and $TSF_{32}G_2$ exhibited minimum ΔE. These results were expected, considering their superhydrophilic tendency and higher photocatalytic activity, as discussed above.

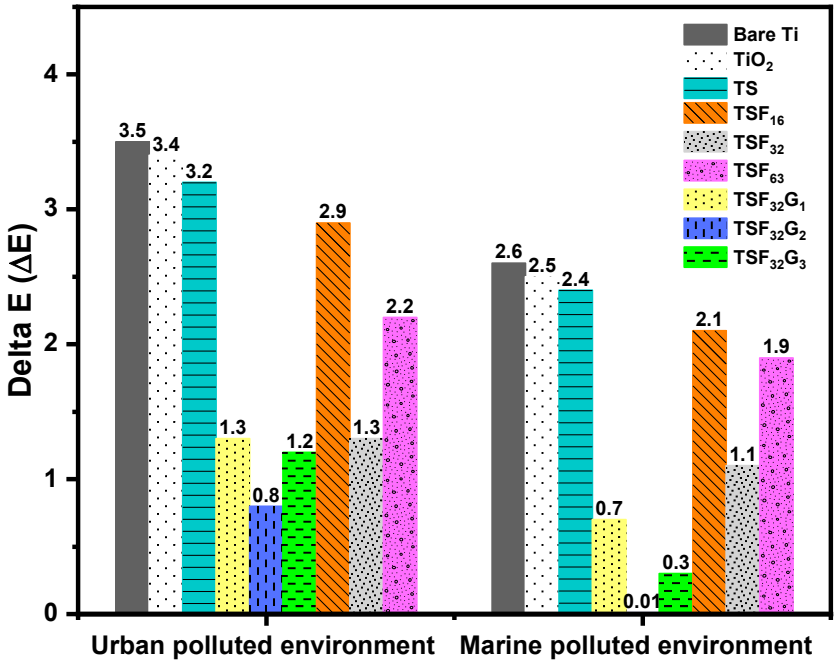

Figure 14. The color difference due to the simulated soiling test for the bare and coated titanium specimens with the mimic urban and marine soils.

Figure 15 demonstrates how a smart coating—for example, the $TSF_{32}G_2$ here presented—could clean the surface from dust and pollutants. Oil content from smog can adhere to the surface easily, and dust particles or contaminants are consequently attracted by the oil and deposit on the surface. After light irradiation (either indoor light or sunlight), the photoactivated surface oxidizes and breaks down the oil components and loosens dust deposits (step 1). In the case of outdoor exposure, then the surface could benefit from rainfall as well to carry away the particles and clean the surface (step 2).

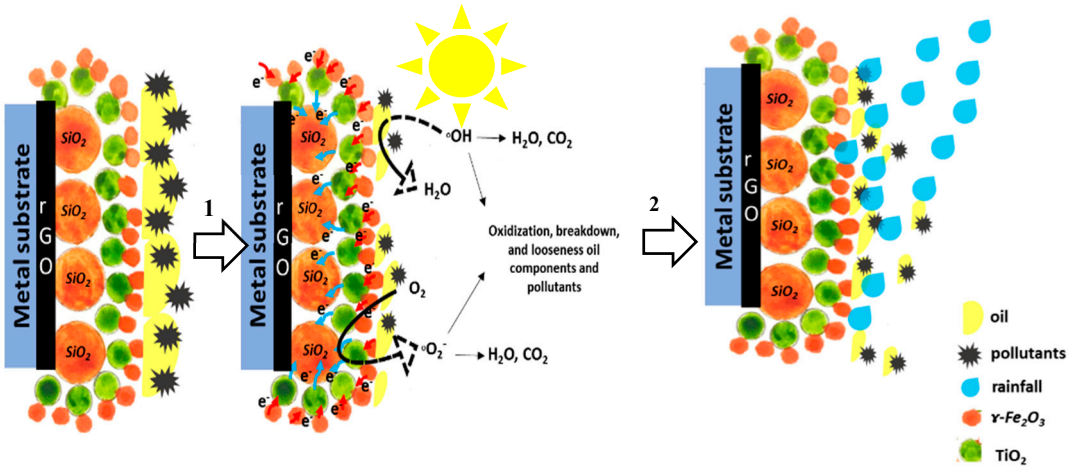

Figure 15. Schematical description of self-cleaning from oil, soil, and pollutants by the photoactive $TSF_{32}G$ (or TSF) coated layers.

4. Conclusions

Different concentrations of γ-Fe_2O_3 and rGO in composite titanium dioxide-silicon dioxide films were synthesized by the sol-gel method and deposited on titanium substrates. The photocatalytic assessment of the TSF and $TSF_{32}G$ coated films indicated that there are optimum contents for γ-Fe_2O_3 and rGO, which are affected by proper anatase/rutile ratio, bandgap and better film morphology with no crack formation; these optimum values were confirmed by wettability analyses, showing the onset of superhydrophilicity only in the composite film also containing rGO. All coated films ensured satisfying transmittance and no appreciable color difference was visible when applied on the substrate. The enhancement of the hydrophilic behavior is ascribable to their R_a, increasing OH groups, and improvement in charge separation efficiency as the rGO layer has an electron acceptor function, improving light harvesting and consequent light-induced wettability conversion. Eventually, the evaluation of self-cleaning performance and discoloration resistance under soiling and acid rain simulations demonstrated that the TSF_{32} and $TSF_{32}G_2$ coated specimens efficiently protect the underlying surface thanks to their excellent self-cleaning performances (resulting from their higher superhydrophilicity and photocatalytic activity) and efficient barrier effect.

Author Contributions: M.M.: Methodology, Investigation, Writing; R.K.: Investigation, Writing; M.B.: Supervision, Resources; M.O.: Investigation; M.V.D.: Project administration, Validation, Writing—review/editing; M.P.: Supervision, Resources. All authors have read and agreed to the published version of the manuscript.

Funding: This work was supported by MIUR, PRIN 2015WBEP3H "Monitoraggio, Consolidamento, Conservazione e Protezione di Beni Culturali".

Conflicts of Interest: The authors declare no conflict of interest.

References

1. Mokhtarifar, M.; Pedeferri, M.P.; Diamanti, M.V. Towards a better preservation of current and future outdoor architectural heritage; maximum suppression of discolouration in anodized and non-anodized titanium sheets. *Environ. Technol. Rev.* **2020**. [CrossRef]

2. Quan, Y.Y.; Zhang, L.Z.; Qi, R.H.; Cai, R.R. Self-cleaning of Surfaces: The role of surface wettability and dust types. *Sci. Rep.* **2016**, *6*. [CrossRef] [PubMed]
3. Kisch, H. Semiconductor photocatalysis-Mechanistic and synthetic aspects. *Angew. Chem. Int. Ed.* **2013**, *52*, 812–847. [CrossRef] [PubMed]
4. Kaneko, M.; Kimura, M.; Tokuno, K. Effects of titanium carbide (TiC) and anodizing voltages on discoloration resistance of colored-titanium sheets. *Corros. Sci.* **2010**, *52*, 1889–1896. [CrossRef]
5. Diamanti, M.V.; Garbagnoli, P.; Curto, B.; Pedeferri, M.P. On the Growth of Thin Anodic Oxides Showing Interference Colors on Valve Metals. *Curr. Nanosci.* **2015**. [CrossRef]
6. Diamanti, M.V.; Aliverti, S.; Pedeferri, M.P. Decoupling the dual source of colour alteration of architectural titanium: Soiling or oxidation? *Corros. Sci.* **2013**, *72*, 125–132. [CrossRef]
7. Kaneko, M.; Takahashi, K.; Hayashi, T.; Muto, I.; Tokuno, K.; Kimura, K. Environmental and metallurgical factors affecting discoloration of titanium sheets in atmospheric environments. *Tetsu-To-Hagane/J. Iron Steel Inst. Jpn.* **2003**, *89*, 833–840. [CrossRef]
8. Pelaez, M.; Nolan, N.T.; Pillai, S.C.; Seery, M.K.; Falaras, P.; Kontos, A.G.; Dunlop, P.S.M.; Hamilton, J.W.J.; Byrne, J.A.; O'Shea, K.; et al. A review on the visible light active titanium dioxide photocatalysts for environmental applications. *Appl. Catal. B Environ.* **2012**, *125*, 331–349. [CrossRef]
9. Keane, D.A.; McGuigan, K.G.; Ibáñez, P.F.; Polo-López, M.I.; Byrne, J.A.; Dunlop, P.S.M.; O'Shea, K.; Dionysiou, D.D.; Pillai, S.C. Solar photocatalysis for water disinfection: Materials and reactor design. *Catal. Sci. Technol.* **2014**, *4*, 1211–1226. [CrossRef]
10. Qu, Y.; Duan, X. Progress, challenge and perspective of heterogeneous photocatalysts. *Chem. Soc. Rev.* **2013**, *42*, 2568–2580. [CrossRef]
11. Seery, M.K.; George, R.; Floris, P.; Pillai, S.C. Silver doped titanium dioxide nanomaterials for enhanced visible light photocatalysis. *J. Photochem. Photobiol. A Chem.* **2007**, *189*, 258–263. [CrossRef]
12. Linic, S.; Christopher, P.; Ingram, D.B. Plasmonic-metal nanostructures for efficient conversion of solar to chemical energy. *Nat. Mater.* **2011**, *10*, 911–921. [CrossRef] [PubMed]
13. Di Paola, A.; García-López, E.; Ikeda, S.; Marc, G.; Ohtani, B.; Palmisano, L. Photocatalytic degradation of organic compounds in aqueous systems by transition metal doped polycrystalline TiO_2. *Catal. Today* **2002**, *75*, 87–93. [CrossRef]
14. Weng, K.W.; Huang, Y.P. Preparation of TiO_2 thin films on glass surfaces with self-cleaning characteristics for solar concentrators. *Surf. Coat.Technol.* **2013**, *231*, 201–204. [CrossRef]
15. Xiao, F.X. Construction of highly ordered ZnO-TiO_2 nanotube arrays (ZnO/TNTs) heterostructure for photocatalytic application. *ACS Appl. Mater. Interfaces* **2012**, *4*, 7055–7063. [CrossRef] [PubMed]
16. Etacheri, V.; Michlits, G.; Seery, M.K.; Hinder, S.J.; Pillai, S.C. A highly efficient $TiO_{2-x}C_x$ nano-heterojunction photocatalyst for visible light induced antibacterial applications. *ACS Appl. Mater. Interfaces* **2013**, *5*, 1663–1672. [CrossRef]
17. Etacheri, V.; Seery, M.K.; Hinder, S.J.; Pillai, S.C. Nanostructured $Ti_{1-x}S_xO_{2-y}N_y$ heterojunctions for efficient visible-light-induced photocatalysis. *Inorg. Chem.* **2012**, *51*, 7164–7173. [CrossRef]
18. Nguyen, P.T.N.; Salim, C.; Kurniawan, W.; Hinode, H. A non-hydrolytic sol-gel synthesis of reduced graphene oxide/TiO_2 microsphere photocatalysts. *Catal. Today* **2014**, *230*, 166–173. [CrossRef]
19. Rezaei, M.; Salem, S. Photocatalytic activity enhancement of anatase-graphene nanocomposite for methylene removal: Degradation and kinetics. *Spectrochim. Acta Part A Mol. Biomol. Spectrosc.* **2016**, *167*, 41–49. [CrossRef]
20. Mokhtarifar, M.; Kaveh, R.; Bagherzadeh, M.; Lucotti, A.; Pedeferri, M.P.; Diamanti, M.V. Heterostructured $TiO_2/SiO_2/\gamma$-Fe_2O_3/rGO Coating with Highly Efficient Visible-Light-Induced Self-Cleaning Properties for Metallic Artifacts. *ACS Appl. Mater. Interfaces* **2020**. [CrossRef]
21. Murphy, A.B. Band-gap determination from diffuse reflectance measurements of semiconductor films, and application to photoelectrochemical water-splitting. *Sol. Energy Mater. Sol. Cells* **2007**, *91*, 1326–1337. [CrossRef]
22. Sleiman, M.; Kirchstetter, T.W.; Berdahl, P.; Gilbert, H.E.; Quelen, S.; Marlot, L.; Preble, C.V.; Chen, S.; Montalbano, A.; Rosseler, O.; et al. Soiling of building envelope surfaces and its effect on solar reflectance—Part II: Development of an accelerated aging method for roofing materials. *Sol. Energy Mater. Sol. Cells* **2014**, *122*, 271–281. [CrossRef]

23. Favez, O.; Cachier, H.; Chabas, A.; Ausset, P.; Lefevre, R. Crossed optical and chemical evaluations of modern glass soiling in various European urban environments. *Atmos. Environ.* **2006**, *40*, 7192–7204. [CrossRef]
24. Abbas, N.; Shao, G.N.; Haider, M.S.; Imran, S.M.; Park, S.S.; Kim, H.T. Sol–gel synthesis of TiO_2–Fe_2O_3 systems: Effects of Fe_2O_3 content and their photocatalytic properties. *J. Ind. Eng. Chem.* **2016**, *39*, 112–120. [CrossRef]
25. Beydoun, D.; Amal, R.; Low, G.K.C.; McEvoy, S. Novel photocatalyst: Titania-coated magnetite. activity and photodissolution. *J. Phys. Chem. B* **2000**, *104*, 4387–4396. [CrossRef]
26. Tobaldi, D.M.; Pullar, R.C.; Gualtieri, A.F.; Seabra, M.P.; Labrincha, J.A. Sol-gel synthesis, characterisation and photocatalytic activity of pure, W-, Ag- and W/Ag co-doped TiO_2 nanopowders. *Chem. Eng. J.* **2013**, *214*, 364–375. [CrossRef]
27. Ghorai, T.K.; Chakraborty, M.; Pramanik, P. Photocatalytic performance of nano-photocatalyst from TiO_2 and Fe_2O_3 by mechanochemical synthesis. *J. Alloys Compd.* **2011**, *509*, 8158–8164. [CrossRef]
28. Hung, W.H.; Chien, T.M.; Tseng, C.M. Enhanced photocatalytic water splitting by plasmonic TiO_2–Fe_2O_3 cocatalyst under visible light irradiation. *J. Phys. Chem. C* **2014**, *118*, 12676–12681. [CrossRef]
29. Xu, Y.J.; Zhuang, Y.; Fu, X. New insight for enhanced photocatalytic activity of TiO_2 by doping carbon nanotubes: A case study on degradation of benzene and methyl orange. *J. Phys. Chem. C* **2010**, *114*, 2669–2676. [CrossRef]
30. Xiong, Z.; Wu, H.; Zhang, L.; Gu, Y.; Zhao, X.S. Synthesis of TiO_2 with controllable ratio of anatase to rutile. *J. Mater. Chem. A* **2014**, *2*, 9291–9297. [CrossRef]
31. Wang, D.; Li, X.; Chen, J.; Tao, X. Enhanced photoelectrocatalytic activity of reduced graphene oxide/TiO_2 composite films for dye degradation. *Chem. Eng. J.* **2012**, *198–199*, 547–554. [CrossRef]
32. Sher Shah, M.S.A.; Park, A.R.; Zhang, K.; Park, J.H.; Yoo, P.J. Green synthesis of biphasic TiO_2-reduced graphene oxide nanocomposites with highly enhanced photocatalytic activity. *ACS Appl. Mater. Interfaces* **2012**, *4*, 3893–3901. [CrossRef] [PubMed]
33. Cheng, H.; Ma, J.; Zhao, Z.; Qi, L. Hydrothermal preparation of uniform nanosize rutile and anatase particles. *Chem. Mater.* **1995**, *7*, 663–671. [CrossRef]
34. Mohamed, H.H. Biphasic TiO_2 microspheres/reduced graphene oxide for effective simultaneous photocatalytic reduction and oxidation processes. *Appl. Catal. A Gen.* **2017**, *541*, 25–34. [CrossRef]
35. Botelho, G.; Andres, J.; Gracia, L.; Matos, L.S.; Longo, E. Photoluminescence and photocatalytic properties of Ag_3PO_4 microcrystals: An experimental and theoretical investigation. *Chempluschem* **2016**. [CrossRef] [PubMed]
36. Bagherzadeh, M.; Kaveh, R. New magnetically recyclable reduced graphene oxide rGO/MFe_2O_4 (M = Ca, Mg)/Ag_3PO_4 nanocomposites with remarkably enhanced visible-light photocatalytic activity and stability. *Photochem. Photobiol.* **2018**. [CrossRef]
37. Ren, W.; Ai, Z.; Jia, F.; Zhang, L.; Fan, X.; Zou, Z. Low temperature preparation and visible light photocatalytic activity of mesoporous carbon-doped crystalline TiO_2. *Appl. Catal. B Environ.* **2007**. [CrossRef]
38. Liu, Y. Hydrothermal synthesis of TiO_2–RGO composites and their improved photocatalytic activity in visible light. *RSC Adv.* **2014**. [CrossRef]
39. Zhang, H.; Lv, X.; Li, Y.; Wang, Y.; Li, J. P25-graphene composite as a high performance photocatalyst. *ACS Nano* **2010**, *4*, 380–386. [CrossRef]
40. Xiang, Q.; Yu, J.; Jaroniec, M. Graphene-based semiconductor photocatalysts. *Chem. Soc. Rev.* **2012**. [CrossRef]
41. Anandan, S.; Narasinga Rao, T.; Sathish, M.; Rangappa, D.; Honma, I.; Miyauchi, M. Superhydrophilic graphene-loaded TIO_2 thin film for self-cleaning applications. *ACS Appl. Mater. Interfaces* **2013**. [CrossRef] [PubMed]
42. Powell, M.J.; Quesada-Cabrera, R.; Taylor, A.; Teixeira, D.; Papakonstantinou, I.; Palgrave, R.G.; Sankar, G.; Parkin, I.P. Intelligent multifunctional VO_2/SiO_2/TiO_2 coatings for self-cleaning, energy-saving window panels. *Chem. Mater.* **2016**. [CrossRef]
43. Uddin, M.J.; Cesano, F.; Scarano, D.; Bonino, F.; Agostini, G.; Spoto, G.; Bordiga, S.; Zecchina, A. Cotton textile fibres coated by Au/TiO_2 films: Synthesis, characterization and self cleaning properties. *J. Photochem. Photobiol. A Chem.* **2008**. [CrossRef]

44. Kesmez, Ö.; Erdem Çamurlu, H.; Burunkaya, E.; Arpaç, E. Sol-gel preparation and characterization of anti-reflective and self-cleaning SiO_2–TiO_2 double-layer nanometric films. *Sol. Energy Mater. Sol. Cells* **2009**. [CrossRef]
45. Munafò, P.; Quagliarini, E.; Goffredo, G.B.; Bondioli, F.; Licciulli, A. Durability of nano-engineered TiO_2 self-cleaning treatments on limestone. *Constr. Build. Mater.* **2014**. [CrossRef]
46. Yamashita, H.; Nakao, H.; Takeuchi, M.; Nakatani, Y.; Anpo, M. Coating of TiO_2 photocatalysts on super-hydrophobic porous teflon membrane by an ion assisted deposition method and their self-cleaning performance. *Nucl. Instrum. Methods Phys. Res. Sect. B Beam Interact. Mater. At.* **2003**. [CrossRef]
47. Graziani, L.; Quagliarini, E.; Bondioli, F.; D'Orazio, M. Durability of self-cleaning TiO_2 coatings on fired clay brick façades: Effects of UV exposure and wet & dry cycles. *Build. Environ.* **2014**. [CrossRef]
48. Calia, A.; Lettieri, M.; Masieri, M. Durability assessment of nanostructured TiO_2 coatings applied on limestones to enhance building surface with self-cleaning ability. *Build. Environ.* **2016**. [CrossRef]
49. Lettieri, M.; Colangiuli, D.; Masieri, M.; Calia, A. Field performances of nanosized TiO_2 coated limestone for a self-cleaning building surface in an urban environment. *Build. Environ.* **2019**. [CrossRef]
50. Shakeri, A.; Yip, D.; Badv, M.; Imani, S.M.; Sanjari, M.; Didar, T.F. Self-cleaning ceramic tiles produced via stable coating of TiO_2 Nanoparticles. *Materials* **2018**, *11*, 1003. [CrossRef]
51. Daryaei, E.; Reza Rahimi Tabar, M.; Moshfegh, A.Z. Surface roughness analysis of hydrophilic SiO_2/TiO_2/glass nano bilayers by the level crossing approach. *Phys. A Stat. Mech. Appl.* **2013**, *392*, 2175–2181. [CrossRef]
52. Dhoke, S.K.; Khanna, A.S. Electrochemical behavior of nano-iron oxide modified alkyd based waterborne coatings. *Mater. Chem. Phys.* **2009**, *117*, 550–556. [CrossRef]
53. Wei, Y.; Zhang, Y.; Gao, X.; Ma, Z.; Wang, X.; Gao, C. Multilayered graphene oxide membrane for water treatment: A review. *Carbon N. Y.* **2018**, *139*, 964–981. [CrossRef]
54. Tsou, C.H.; An, Q.F.; Lo, S.C.; De Guzman, M.; Hung, W.S.; Hu, C.C.; Lee, K.R.; Lai, J.Y. Effect of microstructure of graphene oxide fabricated through different self-assembly techniques on 1-butanol dehydration. *J. Memb. Sci.* **2015**, *477*, 93–100. [CrossRef]
55. Wang, J.; Zhang, Y.; Wang, S.; Song, Y.; Jiang, L. Bioinspired colloidal photonic crystals with controllable wettability. *Acc. Chem. Res.* **2011**, *44*, 405–415. [CrossRef]
56. Wang, J.; Wen, Y.; Hu, J.; Song, Y.; Jiang, L. Fine control of the wettability transition temperature of colloidal-crystal films: From superhydrophilic to superhydrophobic. *Adv. Funct. Mater.* **2007**, *17*, 219–225. [CrossRef]
57. Li, Q.; Guo, Z. Lubricant-infused slippery surfaces: Facile fabrication, unique liquid repellence and antireflective properties. *J. Colloid Interface Sci.* **2019**, *536*, 507–515. [CrossRef]
58. Eshaghi, A.; Dashti, A.; Eshaghi, A.; Mozaffarinia, R. Photo-induced superhydrophilicity of nanocomposite TiO_2–SiO_2 thin film. *Mater. Sci. Pol.* **2011**. [CrossRef]
59. Houmard, M.; Riassetto, D.; Roussel, F.; Bourgeois, A.; Berthomé, G.; Joud, J.C.; Langlet, M. Enhanced persistence of natural super-hydrophilicity in TiO_2–SiO_2 composite thin films deposited via a sol-gel route. *Surf. Sci.* **2008**. [CrossRef]
60. Houmard, M.; Riassetto, D.; Roussel, F.; Bourgeois, A.; Berthomé, G.; Joud, J.C.; Langlet, M. Morphology and natural wettability properties of sol-gel derived TiO_2–SiO_2 composite thin films. *Appl. Surf. Sci.* **2007**. [CrossRef]
61. Fateh, R.; Dillert, R.; Bahnemann, D. Preparation and characterization of transparent hydrophilic photocatalytic TiO_2/SiO_2 thin films on polycarbonate. *Langmuir* **2013**. [CrossRef] [PubMed]
62. Diamanti, M.V.; Gadelrab, K.R.; Pedeferri, M.P.; Stefancich, M.; Pehkonen, S.O.; Chiesa, M. Nanoscale investigation of photoinduced hydrophilicity variations in anatase and rutile nanopowders. *Langmuir* **2013**, *29*, 14512–14518. [CrossRef]
63. Yu, J.C.; Ho, W.; Lin, J.; Yip, H.; Wong, P.K. Photocatalytic activity, antibacterial effect, and photoinduced hydrophilicity of TiO_2 films coated on a stainless steel substrate. *Environ. Sci. Technol.* **2003**, *37*, 2296–2301. [CrossRef]
64. Choi, W.; Termin, A.; Hoffmann, M.R. Effects of metal-ion dopants on the photocatalytic reactivity of quantum-sized TiO_2 particles. *Angew. Chem. Int. Ed. Engl.* **1994**, *33*, 1091–1092. [CrossRef]
65. Choi, W.; Termin, A.; Hoffmann, M.R. The role of metal ion dopants in quantum-sized TiO_2: Correlation between photoreactivity and charge carrier recombination dynamics. *J. Phys. Chem.* **1994**, *98*, 13669–13679. [CrossRef]

66. Yu, J.; Zhou, M.; Yu, H.; Zhang, Q.; Yu, Y. Enhanced photoinduced super-hydrophilicity of the sol-gel-derived TiO_2 thin films by Fe-doping. *Mater. Chem. Phys.* **2006**, *95*, 193–196. [CrossRef]
67. Jin, F.; Lv, W.; Zhang, C.; Li, Z.; Su, R.; Qi, W.; Yang, Q.H.; He, Z. High-performance ultrafiltration membranes based on polyethersulfone- graphene oxide composites. *RSC Adv.* **2013**. [CrossRef]
68. Sakai, N.; Kamanaka, K.; Sasaki, T. Modulation of photochemical activity of titania nanosheets via heteroassembly with reduced graphene oxide. enhancement of photoinduced hydrophilic conversion properties. *J. Phys. Chem. C* **2016**. [CrossRef]
69. Bharti, B.; Kumar, S.; Kumar, R. Superhydrophilic TiO_2 thin film by nanometer scale surface roughness and dangling bonds. *Appl. Surf. Sci.* **2016**, *364*, 51–60. [CrossRef]
70. Wang, R.; Hashimoto, K.; Fujishima, A.; Chikuni, M.; Kojima, E.; Kitamura, A.; Shimohigoshi, M.; Watanabe, T. Light-induced amphiphilic surfaces. *Nature* **1997**, *388*, 431–432. [CrossRef]
71. Lee, H.Y.; Park, Y.H.; Ko, K.H. Correlation between surface morphology and hydrophilic/hydrophobic conversion of MOCVD-TiO_2 films. *Langmuir* **2000**, *16*, 7289–7293. [CrossRef]
72. Sakai, N.; Wang, R.; Fujishima, A.; Watanabe, T.; Hashimoto, K. Effect of ultrasonic treatment on highly hydrophilic TiO_2 surfaces. *Langmuir* **1998**, *14*, 5918–5920. [CrossRef]
73. Feng, X.; Zhai, J.; Jiang, L. The fabrication and switchable superhydrophobicity of TiO_2 nanorod films. *Angew. Chem. Int. Ed.* **2005**, *44*, 5115–5118. [CrossRef] [PubMed]
74. Kim, S.B.; Hwang, H.T.; Hong, S.C. Photocatalytic degradation of volatile organic compounds at the gas-solid interface of a TiO_2 photocatalyst. *Chemosphere* **2002**, *48*, 437–444. [CrossRef]
75. Luo, Z.; Pinto, N.J.; Davila, Y.; Charlie Johnson, A.T. Controlled doping of graphene using ultraviolet irradiation. *Appl. Phys. Lett.* **2012**, *100*. [CrossRef]
76. Duong, D.L.; Han, G.H.; Lee, S.M.; Gunes, F.; Kim, E.S.; Kim, S.T.; Kim, H.; Ta, Q.H.; So, K.P.; Yoon, S.J.; et al. Probing graphene grain boundaries with optical microscopy. *Nature* **2012**, *490*, 235–239. [CrossRef]
77. Zhang, X.; Fan, X.; Yan, C.; Li, H.; Zhu, Y.; Li, X.; Yu, L. Interfacial microstructure and properties of carbon fiber composites modified with graphene oxide. *ACS Appl. Mater. Interfaces* **2012**. [CrossRef]
78. Da, S.X.; Wang, J.; Geng, H.Z.; Jia, S.L.; Xu, C.X.; Li, L.G.; Shi, P.P.; Li, G. High adhesion transparent conducting films using graphene oxide hybrid carbon nanotubes. *Appl. Surf. Sci.* **2017**. [CrossRef]
79. Lu, H.; Yao, Y.; Huang, W.M.; Hui, D. Noncovalently functionalized carbon fiber by grafted self-assembled graphene oxide and the synergistic effect on polymeric shape memory nanocomposites. *Compos. Part B Eng.* **2014**. [CrossRef]
80. Ning, H.; Li, J.; Hu, N.; Yan, C.; Liu, Y.; Wu, L.; Liu, F.; Zhang, J. Interlaminar mechanical properties of carbon fiber reinforced plastic laminates modified with graphene oxide interleaf. *Carbon N. Y.* **2015**. [CrossRef]
81. Son, G.C.; Hwang, D.K.; Jang, J.; Chee, S.S.; Cho, K.; Myoung, J.M.; Ham, M.H. Solution-processed highly adhesive graphene coatings for corrosion inhibition of metals. *Nano Res.* **2019**. [CrossRef]
82. Moon, I.K.; Kim, J., II; Lee, H.; Hur, K.; Kim, W.C.; Lee, H. 2D graphene oxide nanosheets as an adhesive over-coating layer for flexible transparent conductive electrodes. *Sci. Rep.* **2013**. [CrossRef]
83. Akimov, G.Y.; Chaika, E.V.; Marinin, G.A. Wear and fracture toughness of partially stabilized zirconia ceramics under dry friction against steel. *J. Frict. Wear* **2009**. [CrossRef]
84. Paggi, M.; Reinoso, J. An anisotropic large displacement cohesive zone model for fibrillar and crazing interfaces. *Int. J. Solids Struct.* **2015**. [CrossRef]
85. Kajari-Schröder, S.; Kunze, I.; Köntges, M. Criticality of cracks in PV modules. *Energy Procedia* **2012**. [CrossRef]
86. Paggi, M.; Berardone, I.; Infuso, A.; Corrado, M. Fatigue degradation and electric recovery in Silicon solar cells embedded in photovoltaic modules. *Sci. Rep.* **2014**. [CrossRef]
87. Taleb, A.; Mesguich, F.; Hérissan, A.; Colbeau-Justin, C.; Yanpeng, X.; Dubot, P. Optimized TiO_2 nanoparticle packing for DSSC photovoltaic applications. *Sol. Energy Mater. Sol. Cells* **2016**. [CrossRef]
88. Akimov, G.Y.; Chaika, E.V.; Timchenko, V.M.; Marinin, G.A.; Burkhovetskii, V.V. Wear of ceramics based on magnesia- and ceria-stabilized zirconia in dry friction against steel. *J. Frict. Wear* **2009**. [CrossRef]